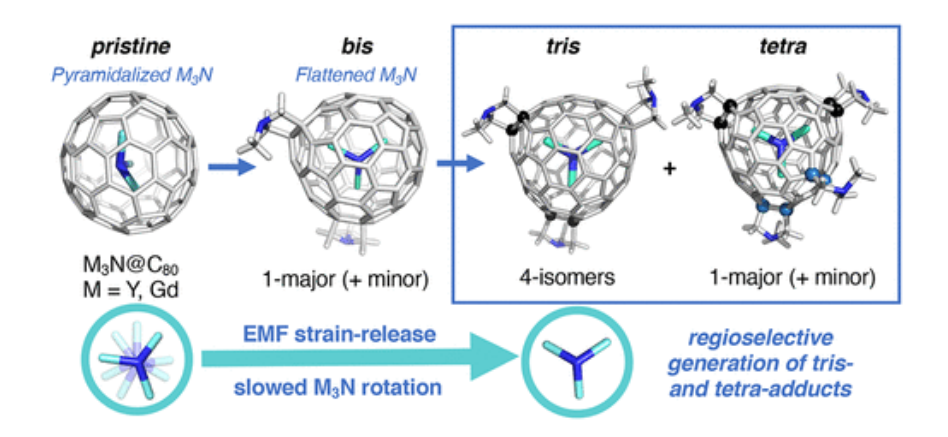
# Regioselective Synthesis and Characterization of Tris- and Tetra-Prato Adducts of M₃N@C80 (M = Y, Gd)

Olesya Semivrazhskaya, Safwan Aroua, Maxim Yulikov, Adrian Romero-Rivera, Steven Stevenson, Marc Garcia-Borràs, Sílvia Osuna\*, and Yoko Yamakoshi\*

#### **Abstract**

The tris- and tetra-adducts of M<sub>3</sub>N@I<sub>h</sub>-C<sub>80</sub> metallofullerenes were synthesized and characterized for the first time. The 1,3-dipolar cycloaddition (Prato reaction) of Y<sub>3</sub>N@I<sub>h</sub>-C<sub>80</sub> and Gd<sub>3</sub>N@I<sub>h</sub>-C<sub>80</sub> with an excess of N-ethylglycine and formaldehyde provided tris- and tetra-fulleropyrrolidine adducts in a regioselective manner. Purification by HPLC and analyses of the isolated peaks by NMR, MS, and vis-NIR spectra revealed that the major products were four tris- and one tetra-isomers for both Y<sub>3</sub>N@I<sub>h</sub>-C<sub>80</sub> and Gd<sub>3</sub>N@I<sub>h</sub>-C<sub>80</sub>. Considering the large number of possible isomers (e.g., at least 1140 isomers for the tris-adduct), the limited number of isomers obtained indicated that the reactions proceeded with high regioselectivity. NMR analyses of the  $Y_3N@I_h$ - $C_{80}$  adducts found that the tris-adducts were all-[6,6]- or [6,6][6,6][5,6]isomers and that some showed mutual isomerization or remained intact at room temperature. The tetraadduct obtained as a major product was all-[6,6] and stable. For the structural elucidation of Gd<sub>3</sub>N@I<sub>D</sub>-C<sub>80</sub> tris- and tetra-adducts, density functional theory (DFT) calculations were performed to estimate the relative stabilities of tris- and tetra-adducts formed upon Prato functionalization of the most pyramidalized regions of the fullerene structure. The most stable structures corresponded to additions on the most pyramidalized (i.e., strained) bonds. Taking together the experimental vis-NIR spectra, NMR assignments, and the computed relative DFT stabilities of the potential tris- and tetra-adducts, the structures of the isolated adducts were elucidated. Electron resonance (ESR) measurements measurements of pristine, bis-, and tris-adducts of Gd<sub>3</sub>N@C<sub>80</sub> suggested that the rotation of the endohedral metal cluster slowed upon increase of the addition numbers to C<sub>80</sub> cage, which is favored for accommodating the Gd atoms of the relatively large Gd<sub>3</sub>N cluster inner space at the sp<sup>3</sup> addition sites. This is presumably related to the high regioselectivity in the Prato addition reaction driven by the strain release of the Gd<sub>3</sub>N@C<sub>80</sub> fullerene structure.



#### Introduction

Chemical functionalization of trimetallic nitride template-endohedral metallofullerenes (TNT-EMFs or  $M_3N@I_{h^-}C_{80}$ , denoted as  $M_3N@C_{80}$ ) have attracted considerable attention for the preparations of new functional materials such as photovoltaic devices(1) and magnetic resonance imaging-contrast agents (MRI-CAs).(2-6) To obtain these materials, it is important to have suitable molecular designs. For instance, the fullerene derivatives with specific addition patterns often display better performance as solar cells by forming a specific orientation or packing of the molecules on the surface of devices.(7) Likewise, MRI-CAs with well-defined structures and controlled chemical functionalization on the fullerene cage are expected to be safer by preventing the release of toxic Gd<sup>3+</sup>, while providing a high enhancement.

Although many reported studies on the chemical conversions of  $M_3N@C_{80}$  have focused on the isolation and characterization of monoaddition products, (8-13) there are a few reports on the bis-addition reactions using Diels–Alder cycloaddition  $(Gd_3N@C_{80})$ , (14) Bingel–Hirsch cyclopropanation  $(Sc_3N@C_{78})$ , (15,16) carbene addition  $(La_2@C_{80})$ , (17,18) or Prato reaction (second addition to  $La@C_{72}(C_6H_3Cl_2)$ ) and direct bis-addition to  $M_3N@C_{80}$  (M = Sc, Lu, Y, Gd, Er)). (20-24) Very interestingly, these bis-addition reactions to  $M_3N@C_{80}$  often proceeded with high regioselectivity. Especially in the case of bis-Prato reactions, which generally do not proceed regioselectively with empty  $I_h$ - $C_{60}$ , (25,26) the bis-adducts of  $M_3N@I_h$ - $C_{80}$  were obtained in a highly regioselective fashion, suggesting an influence from the endohedral  $M_3N$  cluster inside the  $I_h$ - $C_{80}$  cages.

An initial study on Prato bis-additions to M<sub>3</sub>N@C<sub>80</sub> was reported in the presence of larger metal clusters (M = Y, Gd; ionic radii: 0.90, 0.94 Å) to reveal the generation of an asymmetric [6,6][6,6]-isomer as a main adduct for both Y and Gd.(20,27) A separate report by the Echegoyen group on Prato bis-addition reaction of M<sub>3</sub>N@C<sub>80</sub> with smaller metal clusters (M = Sc, Lu; ionic radii: 0.75, 0.86 Å) provided three symmetric isomers ([5,6][5,6]-bis, Sc₃N@C<sub>80</sub>) or two symmetric isomers ([5,6][5,6]- and [5,6][6,6]-bis, Lu<sub>3</sub>N@C<sub>80</sub>).(21-23) These outcomes were explained by the positions of the three endohedral metals of monoadducts estimated by density functional theory (DFT) calculations. (20) In the presence of smaller Sc or Lu, the metal atoms inside monoadducts were located further from the sp<sup>3</sup> addition site, while in the presence of the larger Y or Gd, one of the three metals was directed to the sp<sup>3</sup> addition site of monoadduct. These larger metal clusters (Y<sub>3</sub>N, Gd<sub>3</sub>N) inside the pristine I<sub>h</sub>-C<sub>80</sub> were shown to be pyramidalized by X-ray (0.13 Å (Y), 0.52 Å (Gd))(28,29) and are flatter (less strained) in the monoadduct with increased inner-cage space at sp<sup>3</sup> addition site that can host one of the three endohedral metals. Simultaneously, the movement of M<sub>3</sub>N clusters in monoadducts can be slowed down, and as a consequence, the particular C<sub>80</sub> sp<sup>2</sup> carbons located nearby two other metals of M<sub>3</sub>N become more pyramidalized and strained, priming it for the second Prato addition. These speculations are in line with our recent result on the X-ray crystal structure of a minor symmetric Gd₃N@C<sub>80</sub> bis-adduct having a planar Gd<sub>3</sub>N cluster and showing the coordination of two Gd atoms with inner C<sub>80</sub> cage at two sp<sup>3</sup> addition sites. (24) Following from the previous results on mono-Prato reactions that provided thermodynamic [6,6]- and [5,6]-adducts in a ratio as a function of the size of the metal cluster, (8,13,30-33) it was suggested that the endohedral metal clusters could be used to control the regioselectivity of Prato mono-, bis-, and higher-adducts. However, there are no reports on poly(≥tris) addition reactions of M<sub>3</sub>N@C<sub>80</sub>.

In this study, we report for the first time the tris- and tetra-adducts of  $M_3N@C_{80}$  (M = Y, Gd), obtained by Prato reaction in the presence of a large excess of dipole providing a surprisingly limited number of regioisomers (Figure 1a). The structures of the HPLC-purified adducts (Figure 1b,c) were assigned in part

by  $^1H$ ,  $^{13}C$  NMR for  $Y_3N@C_{80}$  adducts. Based on the vis-NIR spectra of both  $Y_3N@C_{80}$  and  $Gd_3N@C_{80}$  adducts, high similarities in the structures of obtained tris- and tetra-adducts from both  $M_3N@C_{80}$  were found. The fact that the direct precursor bis-adduct for the generation of tris was asymmetric major [6,6][6,6]-bis and observed thermal interconversion of some of the adducts were used for structural analysis. Intensive density functional theory (DFT) calculations were employed for the detailed structural elucidation of tris- and tetra-adducts and to rationalize the origin of the observed regioselectivity. The electron spin resonance (ESR) analyses of  $Gd_3N@C_{80}$  adducts indicated the decrease of movement of the endohedral  $Gd_3N$  cluster upon addition of pyrrolidine moieties on  $C_{80}$  cage, in good agreement with the DFT calculations that showed the larger Gd metals pointing toward the  $Sp^2$  addition site being hosted by aromatic rings of  $C_{80}$  cage.

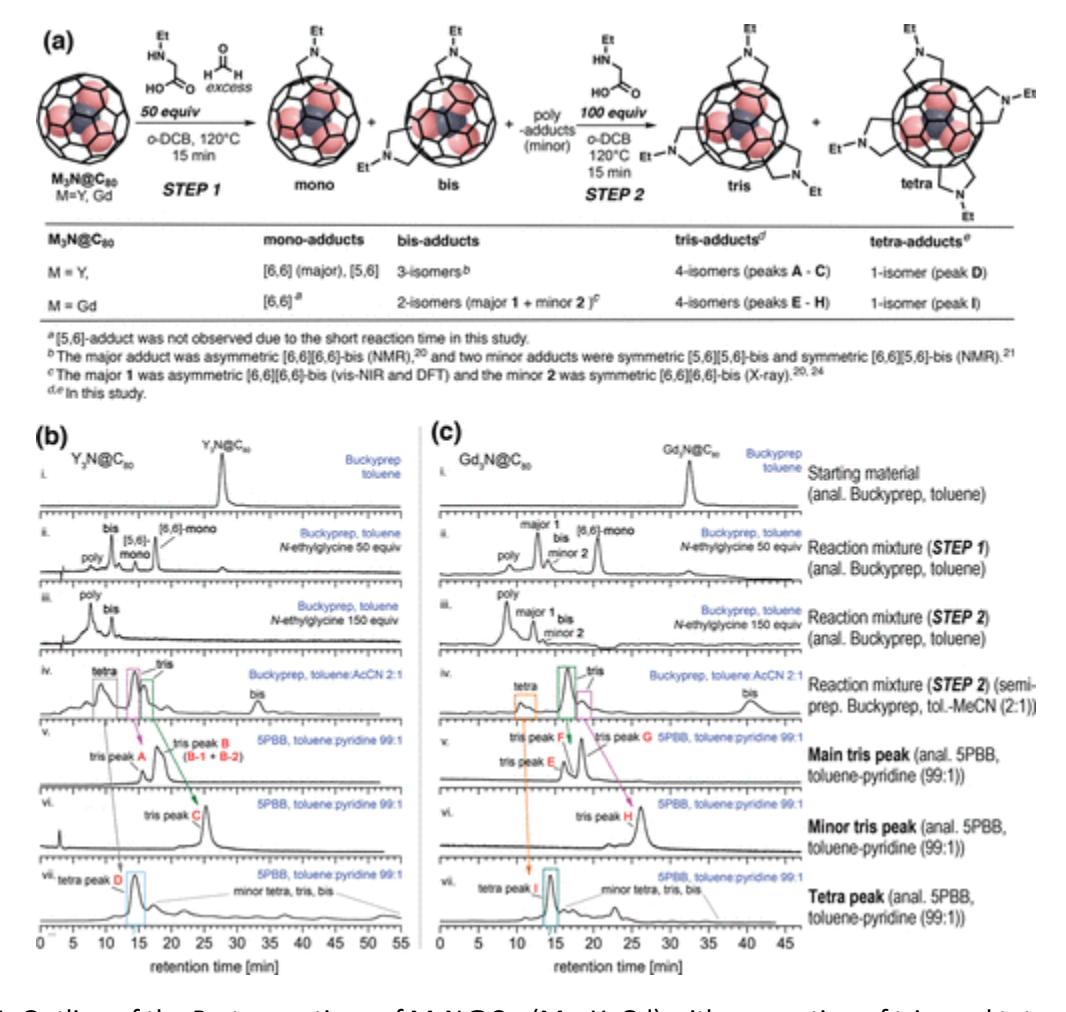


Figure 1. Outline of the Prato reactions of  $M_3N@C_{80}$  (M = Y, Gd) with generation of tris- and tetra-adducts (a) and corresponding HPLC peaks (b, c). (a) Prato reactions of  $M_3N@C_{80}$  (M = Y, Gd) with 50 equiv of *N*-ethylglycine (STEP 1, to generate mainly mono- and bis-adducts) and subsequent addition of 100 equiv of *N*-ethylglycine (STEP 2, for the generation of tris- and tetra-adducts). Reagents and conditions: (STEP 1) *N*-ethylglycine (50 equiv), formaldehyde (400 equiv), *o*-dichlorobenzene, 120 °C, 15 min; (STEP 2) *N*-ethylglycine (additional 100 equiv), 120 °C, additional 15 min. (b, c) HPLC diagrams of reaction process (i–iii) (Buckyprep 4.6 mm i.d. × 250 mm, toluene, 1.0 mL/min, 390 nm) and purification process (iv–vii) of tris- and tetra-peaks **A**–**D** for  $Y_3N@C_{80}$  (b) and **E**–**I** for  $Gd_3N@C_{80}$  (c). (iv) Purification by semiprep HPLC

(Buckyprep 10 mm i.d.  $\times$  250 mm, toluene-acetonitrile (2:1), 5.0 mL/min, 390 nm) and (v–vii) subsequent purification by analytical HPLC (5PBB 4.6 mm i.d.  $\times$  250 mm, toluene-pyridine (99:1), 1.0 mL/min, 390 nm).

## **Experimental Section**

## General

NMR spectra were recorded on Bruker 600 spectrometer equipped with a CryoProbe (Bruker BioSpin GmbH; Rheinstetten, Germany). MALDI-MS spectra were recorded in a negative mode on a Microflex LRF model MALDI-TOF mass spectrometer (N<sub>2</sub>-laser, 337 nm, 3 ns pulse) (Bruker Daltonics GmbH, Bremen, Germany) using 2-trans-[3-(4-tert-butylphenyl)-2-methyl-2-propenilyden]malononitrile (DCTB, 98%, Sigma-Aldrich) as a matrix, in a molar ratio above 1000:1 (matrix-to-analyte) in probes. ESI-MS spectra were recorded in a positive mode on a DIONEX Ultimate 3000 RSLC ESI MS (Thermo Fischer Scientific, Inc., Sunnyvale, CA, USA) and on a Bruker maXis ESI (Bruker Daltonics) for high resolution. The vis-NIR spectra were recorded on a JASCO V-570 spectrophotometer. HPLC analyses were carried out by a JASCO PU-2080 PlusHPLC pump, JASCO MD-2018 Plus detector, and ChromNAV Chromatography Data System (JASCO Co., Tokyo, JPN) with Buckyprep columns (analytical and semipreparative) or 5BPP column (analytical) from Nakalai Tesque (Kyoto, JPN). All the solvents used were in HPLC grade and were purchased from Acros Organic (Thermo Fischer Scientific, Inc., Geel, Belgium). All the reagents were purchased from corresponding suppliers and purified as described when needed. All the M<sub>3</sub>N@C<sub>80</sub> compounds were purchased from Luna Innovations (Roanoke, VA, USA).

## General Procedure for the Prato Reaction of M<sub>3</sub>N@I<sub>h</sub>-C<sub>80</sub> (M = Y, Gd)

A solution of a mixture of  $M_3N@I_h-C_{80}$  (10 mg, 8.1 or 6.9 µmol, 1.0 equiv), *N*-ethylglycine (50 equiv), and paraformaldehyde (400 equiv) in *o*-dichlorobenzene (50 mL) was treated under sonication for 5 min. Nitrogen gas was bubbled through the solution for 5 min to remove oxygen. The reaction mixture was stirred at 120 °C for 15 min (STEP 1 in Figure 1a) and reaction process was checked by HPLC (Buckyprep 4.6 mm i.d. × 250 mm, toluene, 1.0 mL/min, 390 nm, Figure 1b,c-ii). Subsequently, additional 100 equiv of *N*-ethylglycine was added to the reaction mixture and heated for additional 15 min (STEP 2 in Figure 1a) and checked by HPLC (Figure 1b,c-iii). The solvent was removed under reduced pressure to ca. 0.5 mL, and the residue was dissolved in a mixture of toluene-acetonitrile (2:1, 4.5 mL) and filtered over a 0.22 mm filter before subjecting to the HPLC purification using Buckyprep column (10 mm i.d. × 250 mm, toluene-acetonitrile (2:1), 5.0 mL/min, 390 nm, Figure 1b,c-iv). The major fractions were collected and subjected to further purification by 5PBB column (4.6 mm i.d. × 250 mm, toluene-pyridine (99:1), 1.0 mL/min, 390 nm, Figure 1b,c-v-vii). The solvents were removed and dried under vacuum to provide the isolated products (additional details are given in the SI).

#### **Computational details**

All density functional theory (DFT) calculations were performed with the Amsterdam Density Functional (ADF) program. (34,35) The molecular orbitals (MOs) were expanded in an uncontracted set of Slater-type orbitals (STOs) of triple- $\zeta$  (TZP) quality containing diffuse functions and one set of polarization functions. An auxiliary set of s, p, d, f, and g STOs was used to fit the molecular density and to represent the Coulomb and exchange potentials accurately for each SCF cycle. Energies and gradients were calculated using the local density approximation (Slater exchange and VWN correlation)(36) with nonlocal corrections for

exchange (Becke88)(37) and correlation (Perdew86)(38) included self-consistently (i.e., the BP86 functional). All calculations reported here were performed considering the antiferromagnetic coupling (i.e., 7 unpaired electrons S = 7/2) for gadolinium. Scalar relativistic corrections were included self-consistently using the zeroth order regular approximation (ZORA).(39)Moreover, energy dispersion corrections were introduced using Grimme's methodology(40,41) (D2) as implemented in ADF 2010.01 version.(34,35) All the structures were fully optimized using these corrections in each optimization step. It was shown that dispersion corrections are essential for a correct description of the thermodynamics and kinetics of fullerene.(42,43) The actual geometry optimizations were performed with the QUantum-regions Interconnected by Local Descriptions(44) (QUILD) program, which functions as a wrapper around the ADF program. The QUILD program constructs all input files for ADF, runs ADF, and collects all data; ADF is used only for the generation of the energy and gradients. The starting orientation for the metallic cluster (both planar and pyramidalized) is taken from the orientations from the bis-adduct calculations and X-ray data previously reported.(20,24)

## **ESR Experiment**

The ESR measurements were performed on a commercial Bruker ElexSys EPR spectrometer operating at 9.43 GHz microwave frequency, with a rectangular TE102 mode commercial resonator probe-head (Bruker). Sample temperature was stabilized with a liquid-nitrogen flow cryostate. ESR spectra were recorded at 20 mW incident microwave power (10 dB attenuation), 0.1 mT magnetic field modulation, and 100 kHz magnetic field modulation frequency. Each Gd<sub>3</sub>N@C<sub>80</sub> material (pristine, a mixture of bisadducts, or tris-adducts) was placed in a thin-wall quartz capillary with 3 mm outer diameter as a powder for the measurements.

#### **Results and Discussion**

#### Prato Reactions of Y₃N@C<sub>80</sub> and Gd₃N@C<sub>80</sub> and Purification of Tris- and Tetra-Adducts

Prato reactions of  $Y_3N@C_{80}$  or  $Gd_3N@C_{80}$  were carried out in the presence of a large excess of *N*-ethylglycine (150 equiv) and paraformaldehyde (400 equiv) in *o*-dichlorobenzene at 120 °C (<u>Figure 1</u>a). Since it is known that mono-Prato adducts of  $Y_3N@C_{80}$  and  $Gd_3N@C_{80}$  undergo [6,6]-to-[5,6] isomerization via a 1,5-sigmatoropic rearrangement with  $t_{1/2}$  of ca. 150 and 400 min at 120 °C,(<u>31)</u> each reaction was stopped after short intervals (<30 min) to observe predominantly the kinetic products. The reaction was carried out first with 50 equiv of *N*-ethylglycine for 15 min (STEP 1). After the reaction mixture was checked by HPLC (<u>Figure 1</u>b,c-ii) to confirm that the starting materials were largely consumed to provide the mono- and bis-adducts as major products, the reaction was maintained in the presence of an additional 100 equiv of *N*-ethylglycine for an additional 15 min at 120 °C (STEP 2). The starting materials and monoadducts disappeared and increases of poly-adducts peaks were observed in both  $Y_3N@C_{80}$  and  $Gd_3N@C_{80}$  (<u>Figure 1</u>b,c-iii). ESI-MS confirmed that main contents of reaction mixture were tris- and tetra-adducts with minor amounts of bis- and penta-adducts (<u>Figure 2</u>a,b-i).(<u>45)</u> Both reaction mixtures were subjected to HPLC purification.

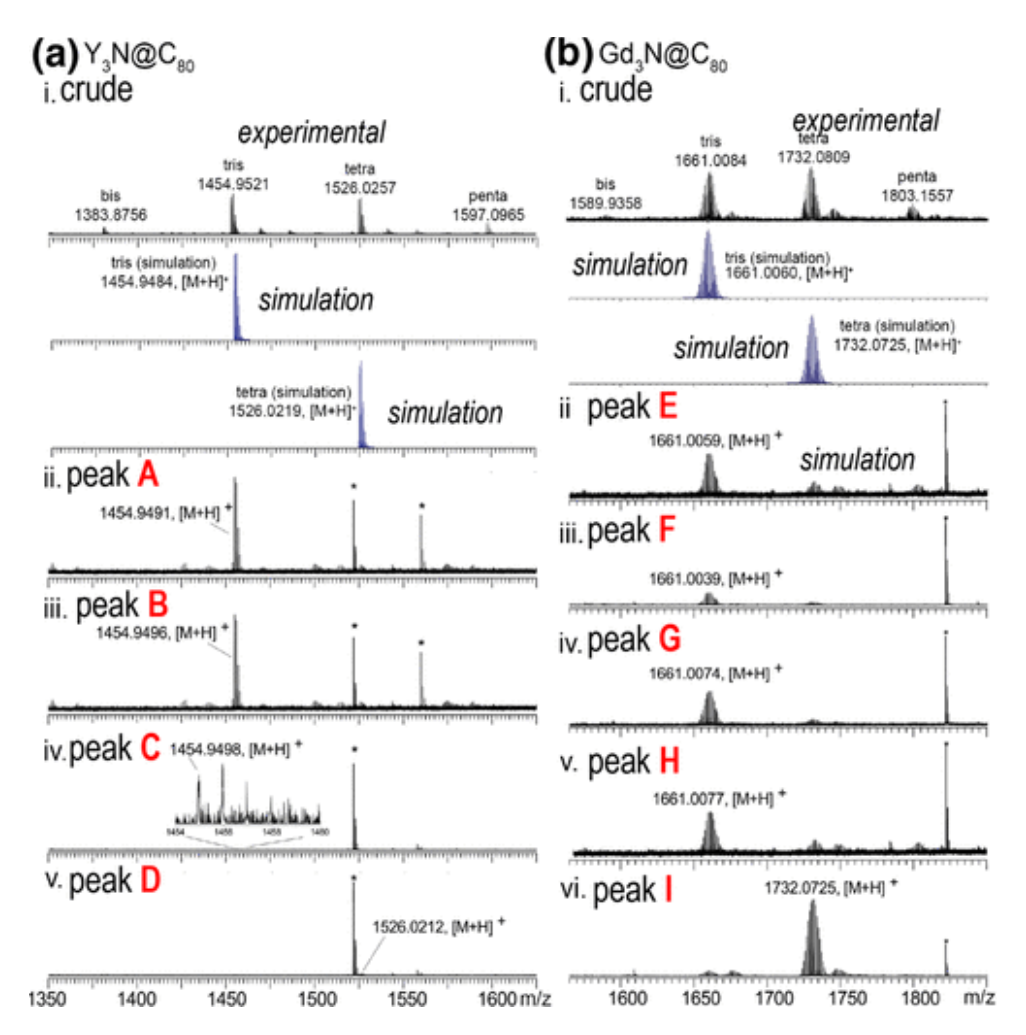


Figure 2. Positive-ion ESI-MS of the crude mixture of Prato reactions of and  $Y_3N@C_{80}$  (a-i) and  $Gd_3N@C_{80}$  (b-i) and separated peaks **A–D** for  $Y_3N@C_{80}$  (a-ii–v) and peaks **E–I** for  $Gd_3N@C_{80}$  (b-ii–vi). \*Calibration standards.

The HPLC purification was carried out first using a semipreparative Buckyprep column and toluene-MeCN (2:1) (<u>Figure 1</u>b,c-iv). Successfully separated tris- (two fractions) and tetra-adducts (one fraction) were further purified using an analytical 5PBB column with toluene-pyridine (99:1). As shown in <u>Figure 1</u>b-v,vi, three peaks **A–C** (containing four isomers),(<u>46</u>) corresponding to the tris-adducts of  $Y_3N@C_{80}$ , were separated. Interestingly, from the tetra-adduct fraction in <u>Figure 1</u>b-iv, only one major tetra-adduct peak **D** was observed by 5PBB HPLC (<u>Figure 1</u>b-vii). A very similar situation was observed in the reaction of  $Gd_3N@C_{80}$ , which provided four tris-adduct peaks **E–H** and one major tetra-adduct peak **I**. After all the purified peaks were confirmed by ESI- and MALDI-MS (<u>Figures 2</u>a,b; <u>S1–S3</u>; and <u>S26–S28</u>), the peaks **A–D** from  $Y_3N@C_{80}$  were subjected to NMR analyses.

# <sup>1</sup>H and <sup>13</sup>C NMR Analyses of Tris- and Tetra-Adducts of Y<sub>3</sub>N@C<sub>80</sub>

As described above, four tris-adducts isomers and one major tetra-adduct isomer were obtained from both  $Y_3N@C_{80}$  and  $Gd_3N@C_{80}$ . Considering that >1140 and >4800 types of tris- and tetra-adducts are

possible in terms of geometry of the  $I_h$ -C<sub>80</sub> molecule, these limited numbers for tris- and tetra-adducts obtained suggested that oligo-Prato reactions of M<sub>3</sub>N@C<sub>80</sub> (M = Y, Gd) proceeded in a highly regioselective manner. To obtain structural information on these tris- and tetra-adducts in part, especially the addition pattern ([6,6] or [5,6]), NMR analyses of Y<sub>3</sub>N@C<sub>80</sub> adducts (**A**–**D**) were performed. Based on the numbers of pyrrolidine CH<sub>2</sub> protons and numbers of ethyl CH<sub>2</sub> protons, the peaks **A**, **C**, and **D** consisted of a single isomer, while peak **B** was a mixture of two tris-isomers (namely **B-1** and **B-2**) (Figures 3 and 4), as described in detail below.

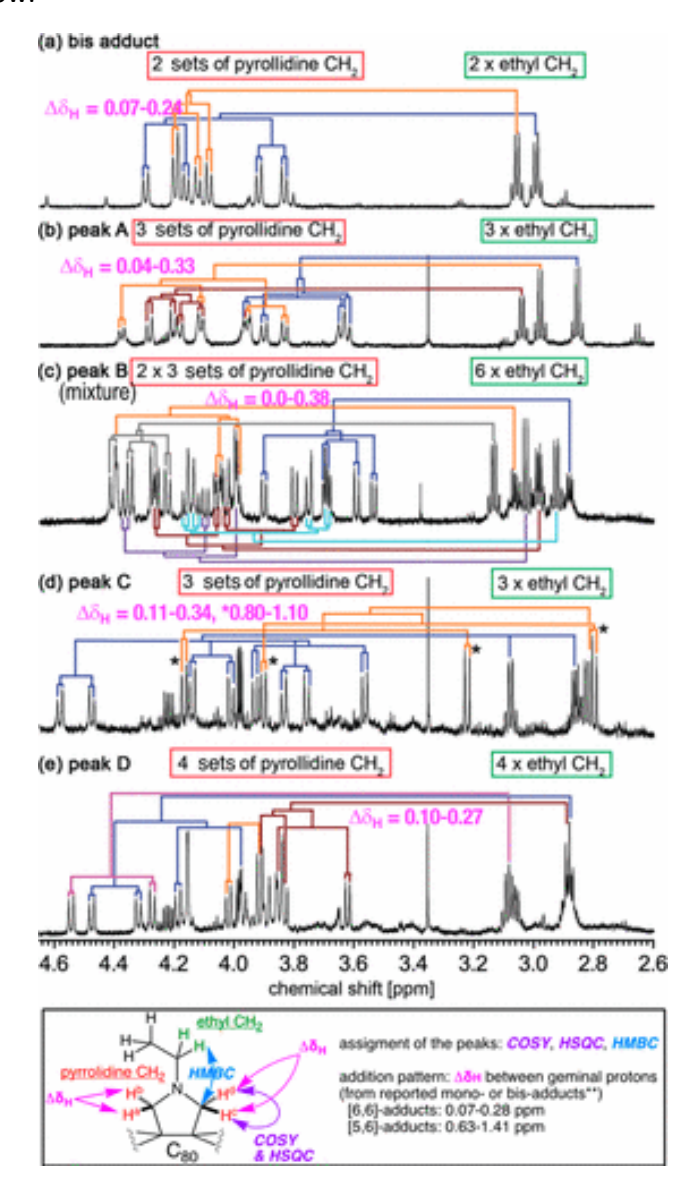


Figure 3.  $^1$ H NMR spectra of Prato adducts of  $Y_3N@C_{80}$  (in CDCl<sub>3</sub>, 600 MHz). (a) Major bis-adduct as a standard (asymmetric [6,6][6,6]-adduct); (b) tris-adduct **A**; (c) tris-adducts **B** (a mixture of **B-1** and **B-2**); (d) tris-adduct **C** (\* $\Delta\delta_H$  value indicating one [5,6]-addition); and (e) tetra-adduct **D**. The signals marked by the individual color line correspond to each pyrrolidine moiety, as assigned on the basis on the COSY, HSQC, and HMBC NMR spectra (all spectra are provided in the <u>SI</u>). The bottom figure shows assignment strategy based on  $\Delta\delta_H$  (\*\* $\Delta\delta_H$  values are from the previous reports)(20–22,31) and 2D NMRs.

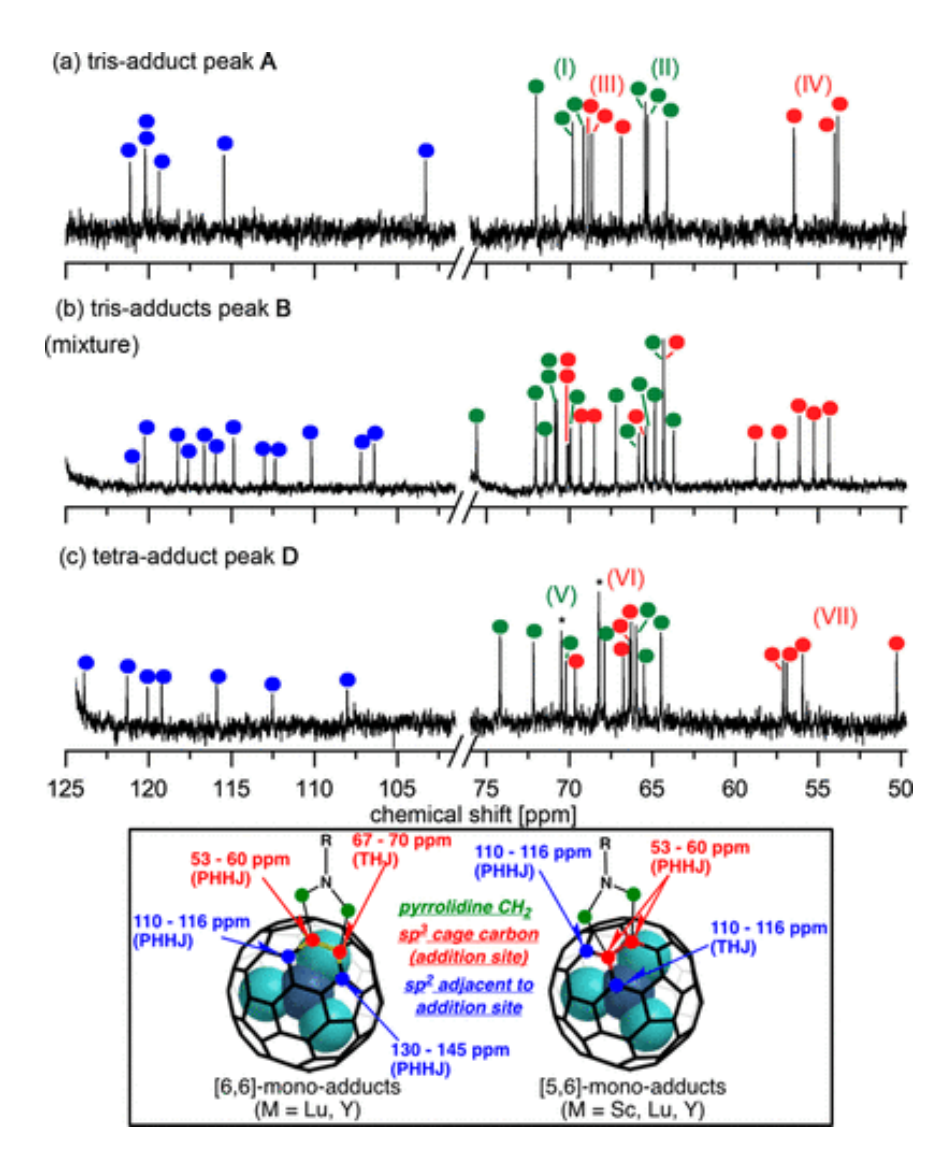


Figure 4.  $^{13}$ C NMR spectra of tris-adducts **A** (a), **B** (b), and tetra-adduct **D** (c) of  $Y_3N@C_{80}$  in the key regions of 100–130 and 50–75 ppm. The five peaks instead of six in the range 52–60 ppm in (b) and seven peaks instead of eight in 63–75 ppm are due to the overlapping of two peaks in (c). Bottom figure is the typical  $^{13}$ C NMR patterns of [6,6]- and [5,6]-monoadducts. The peaks for impurities are marked with asterisks.

#### NMR Analysis of Peak A

In the  $^1$ H NMR spectrum of peak **A** (<u>Figure 3</u>b), 12H pyrrolidine methylene protons (three pairs of four doublets) and 6H of methylene protons for *N*-ethyl groups (three quartets) were observed, suggesting that peak **A** is a single isomer with an asymmetric tris-adduct structure. The connections between each pyrrolidine and ethyl groups (<u>Figure 3</u>b) were assigned by two-dimensional (2D) NMR (<u>Figures S6–S9</u>). The  $^{13}$ C NMR spectrum of peak **A** (<u>Figure 4</u>a) revealed 74 signals in the region for sp<sup>2</sup> C<sub>80</sub> carbons (100–160 ppm, <u>Figure S5</u>) and 6 signals corresponding to sp<sup>3</sup> addition sites (52–73 ppm, signals III and IV in red, <u>Figure 4</u>a) confirming the asymmetry of the molecule. This was in line with the pyrrolidine CH<sub>2</sub> signals,

which were observed as 6 peaks (I and II in green in Figure 4a) in the <sup>13</sup>C NMR (assignment was in combination with HMBC and HSQC). As depicted in the bottom picture in Figure 4, it is known that the sp³ junction carbon is in general observed over 65 ppm for the triple hexagon junction (THJ) and below 60 ppm for the pentagon-hexagon-hexagon junction (PHHJ).(30) Based on this, we assigned all three addition sites to [6,6]-junctions (one THJ and one PHHJ carbons). Furthermore, the apparent spectral pattern of 12 sp² carbons adjacent to the sp³ addition site was in the high field region (103–122 ppm, 6 signals in blue in Figure 4a), and the downfield peaks (130–145 ppm, other 6 signals) indicated that the three addition sites of **A** were all [6,6] (please refer the numbers in the structure of [6,6]-adduct in the bottom picture of Figure 4). Taken together, the <sup>1</sup>H and <sup>13</sup>C NMR data indicated the tris-adduct **A** was an asymmetric [6,6][6,6]-tris-isomer.

## NMR Analysis of Peak B

As indicated in the analytical HPLC peak with a shoulder, the  $^1\text{H}$  and  $^{13}\text{C}$  NMR of peak **B** clearly suggested that it was a mixture of two tris-isomers (**B-1** and **B-2**) (Figure 1b-v). In the  $^1\text{H}$  NMR (Figure 3c), the signals for the pyrrolidine methylenes were observed as 6 sets of 2-coupled doublets (in total 24-H). Based on the previous studies on mono- and bis-adducts showing that  $\Delta\delta_H$  values of geminal H (Ha versus Hb and Hc versus Hb) are generally larger in case of [5,6]-adduct (ca. 0.6–1.4 ppm) and relatively smaller in the case of [6,6]-adduct (ca. 0.1–0.3 ppm),(20–22) it is likely that both isomers **B-1**, **2** had the [6,6][6,6][6,6]-tris structure. Furthermore, in the  $^{13}$ C NMR of **B** (Figure 4b), peaks corresponding to the sp3 carbons on the addition site were observed in two separate regions, such as a higher field at 54–59 ppm (5 signals with one overlapping) and a lower field at 65–72 ppm (6 signals, marked with red) in good agreement with reported [6,6]-adducts (one peak at 67–70 ppm and the other at 53–60 ppm, depicted in the bottom picture of Figure 4). The  $^{13}$ C NMR signals for the sp2 cage carbons adjacent to the addition sites (marked with blue) were found in two separate regions: 12 signals in 105–122 ppm and 12 signals in 125–145 pm, in line with the general observation for the [6,6]-adducts (bottom picture of Figure 4). These data supported the assignment of peak **B** as a mixture of two asymmetric all-[6,6] tris-adducts.

## NMR Analysis of Peak C

The NMR spectra of peak  $\bf C$  revealed that it contains one asymmetric tris-isomer, presumably with the [6,6][6,6][5,6]-structure. In detail, the  $^1$ H NMR spectrum (Figure 3d) revealed that  $\Delta\delta_H$  values of geminal CH<sub>2</sub> protons of one pyrrolidine (marked with asterisks in Figure 3d) were 0.99 and 1.04 ppm, indicating that one of the addition sites was on a [5,6]-junction, while the other two addition sites were on [6,6]-junctions, with smaller  $\Delta\delta_H$  values of geminal pyrrolidine CH<sub>2</sub> protons (0.1–0.3 ppm).(20–22) Unfortunately, the  $^{13}$ C NMR spectrum of  $\bf C$  was not available due to the limited amount of product obtained.

## NMR Analysis of Peak D

In the case of peak **D**, four sets of pyrrolidine groups were observed separately in the <sup>1</sup>H NMR spectrum indicating that peak **D** contained a single asymmetric tetra-isomer. By the analysis of the <sup>13</sup>C NMR chemical shifts for sp<sup>3</sup> carbons on addition sites and their adjacent sp<sup>2</sup> carbons (<u>Figure 4</u>c), peak **D** was assigned as the all-[6,6] tetra-adduct. In the <sup>13</sup>C NMR, peaks corresponding to the sp<sup>3</sup> addition site were observed in two separate regions, one in downfield at 67–70 ppm (4 peaks VI in red) and the other in upfield at 50–57 ppm (4 peaks VII in red). Furthermore, seven sp<sup>2</sup> carbon peaks (blue peaks in <u>Figure 4</u>c, additional one being overlapped with the solvent peak) were observed and assigned as adjacent carbons

to the addition site in the range of 105–125 ppm, further supporting the conjecture that all addition sites were of the [6,6]-type. This elucidation was in good agreement to the smaller  $\Delta\delta_H$  values of geminal pyrrolidine CH<sub>2</sub> peaks observed in <sup>1</sup>H NMR (<u>Figure 3</u>e).

## **Vis-NIR Analysis**

The vis-NIR spectra were obtained from the photodiode array detector of HPLC (eluent: toluene) (<u>Figure 5</u>). Each peak for the tris- or tetra-adduct showed an unique absorption pattern and mostly can correlate the analogous isomers between  $Y_3N@C_{80}$  and  $Gd_3N@C_{80}$ . As shown in <u>Figure 5</u>, identical absorption patterns were observed in the pair of peaks **A** and **E**, **B-1** and **G**, **C** and **H**, and **D** and **I**, indicating presumably the same  $C_{80}$  chromophore with same addition site between these pairs. Based on the addition patterns ([6,6] or [5,6]) of  $Y_3N@C_{80}$  adducts indicated by NMR as above, addition patterns of adducts for  $Gd_3N@C_{80}$  (peaks **E** and **G-I**) were speculated as summarized in <u>Table 1</u>.

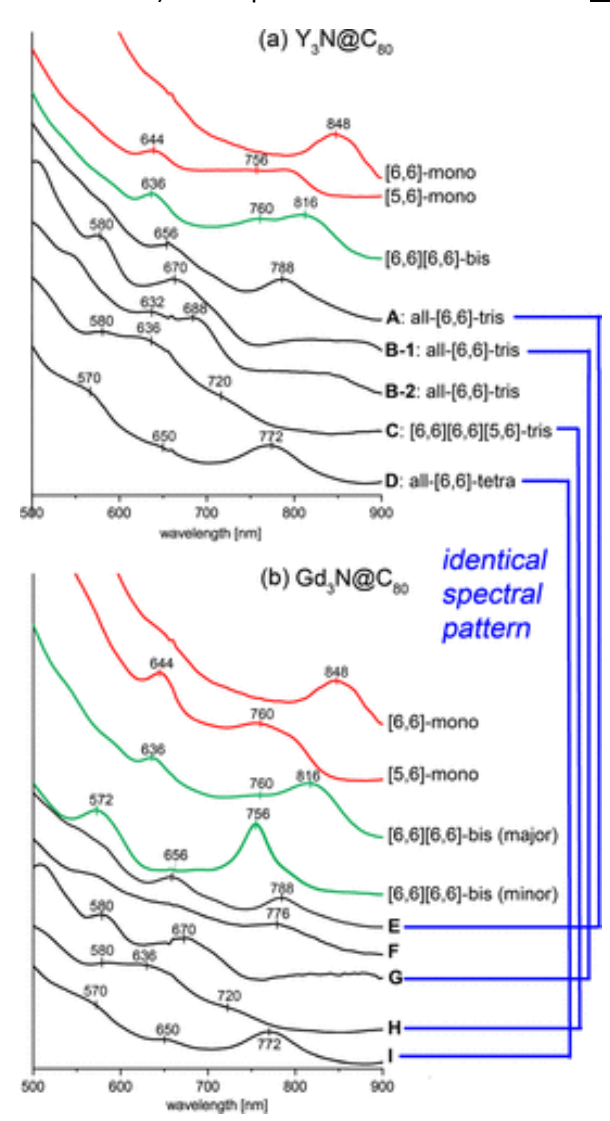


Figure 5. Vis-NIR spectra of Prato adducts of  $Y_3N@C_{80}$  (a) and  $Gd_3N@C_{80}$  (b). The spectra were recorded on a HPLC PDA detector with toluene as an eluent.

Table 1. List of the Obtained Adducts of Y₃N@C<sub>80</sub> and Gd₃N@C<sub>80</sub> with Their Structural Information

peaks	addition sites	properties
Y <sub>3</sub> N@C <sub>80</sub>		
bis	[6,6][6,6] <sup>a</sup>	asymmetric, direct precursor for A-D
A (tris) B-1 (tris) B-2 (tris)	all-[6,6] <sup>a</sup> all-[6,6] <sup>a</sup> all-[6,6] <sup>a</sup>	all asymmetric, <b>A</b> and a mixture of <b>B</b> -1, <b>2</b> interconvert each other
C (tris)		asymmetric, stable
D (tetra)	all-[6,6] <sup>a</sup>	asymmetric, stable
Gd <sub>3</sub> N@C <sub>80</sub>		
major bis-1	$[6,6][6,6]^b$	identical vis-NIR to major-bis of Y <sub>3</sub> N@C <sub>80</sub> , direct precursor for <b>E-I</b>
minor bis-2	[6,6][6,6] <sup>c</sup>	C <sub>2</sub> -symmetric, thermally isomerizes to
		major bis-1
E (tris)	all-[6,6] <sup>b</sup>	identical vis-NIR to <b>A</b> , interconverts
		with ${f G}$
F (tris)	unknown	stable
G (tris)	all-[6,6] <sup>b</sup>	identical vis-NIR to <b>B-1</b> , intercon-
		verts with <b>E</b>
H (tris)	$[6,6][6,6][5,6]^{t}$	dentical vis-NIR to <b>C</b> , stable
I (tetra)	all-[6,6] <sup>b</sup>	identical vis-NIR to <b>D</b> , stable
	(Y <sub>3</sub> N@C <sub>80</sub> ) major asymmetric bis-addu ((6,6)[6,6]) (by NMR, DFT)  (Gd <sub>3</sub> N@C <sub>80</sub> ) major asymmetric bis-addu bis-1 ((6,6)[6,6)) (by vis-NIR, DFT)	B-1,2 (all-[6,6]) - Isom.  C ([6,6][6,6][5,6]) = stable  tetra-adduct:  D (all-[6,6]) = stable   tris-adducts:  E (all-[6,6]) - Isom.

<sup>&</sup>lt;sup>a</sup> Based on NMR spectra.

The bottom figure is the summary.

<sup>&</sup>lt;sup>b</sup> Based on vis-NIR identical to Y<sub>3</sub>N@C<sub>80</sub> adduct.

<sup>&</sup>lt;sup>c</sup> Based on X-ray diffraction in the previous study. (24)

#### **Generation of Tris-Adducts from Bis-Adducts**

In the structural elucidation of tris- and tetra-adducts, one of the most important information is the structure of the starting material (bis-adduct). Using two types of bis-adducts of  $Gd_3N@C_{80}$  ([6,6][6,6]-asymmetric major-bis-1 and [6,6][6,6]-symmetric minor-bis-2) as starting materials, the generation of poly-adducts was investigated by HPLC.(20,24) As shown in <u>Figure 6a</u> (<u>Figure S29</u>, in detail) in the reaction using major-bis-1 as a starting material, poly-adducts were generated directly, while the reaction of minor-bis-2 did not directly provide poly-adducts and only after initial thermal isomerization of minor-bis-2 to major-bis-1 (<u>Figures 6b</u> and <u>S30</u>). These results indicate that major-bis-1 was a direct precursor to the tris- and tetra-adducts. A similar situation was observed for the synthesis of tris- and tetra-adducts of  $Y_3N@C_{80}$  directly from the asymmetric bis-adduct (analogous molecule for major-1 of  $Gd_3N@C_{80}$ ), providing the same ratio of products as direct reaction to  $Y_3N@C_{80}$  (<u>Figure S25</u>). These results suggested that the structures of the tris- and tetra-adducts obtained in this study correspond to one or two more additions to the major bis-adducts and subsequent isomerization products (<u>Figure 6c</u>).

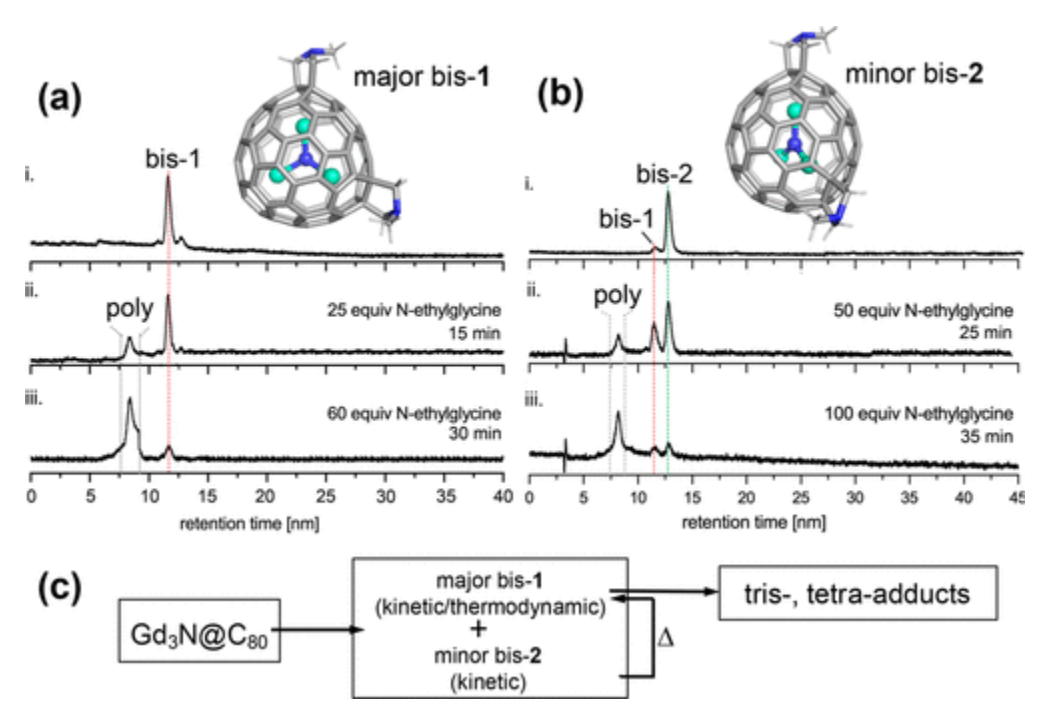


Figure 6. Generation of tris- and tetra-Prato adducts of  $Gd_3N@C_{80}$  from major-bis-adduct **1** (a) or minor-bis-adduct **2** (b) and estimated reaction pathway in tris-, tetra-adducts generation from major asymmetric bis-**1** (c). HPLC conditions: Byckyprep column (4.6 mm i.d. × 250 mm), 1.0 mL/min, eluent: toluene. The structures of major-bis-**1** (asymmetric) and minor-bis-**2** (symmetric) are based on a previous report. (24)

#### **Mutual Isomerization of Tris-Adducts**

It is known that Prato monoadducts of  $M_3N@C_{80}$  exhibit [6,6]-to-[5,6] isomerization via sigmatropic rearrangement dependent on the relative thermodynamic stability of each isomer. (8,13,31,47) In the present study, a similar isomerization was observed between some of the isolated tris-adducts. As shown in <u>Figures 7</u>a,b and <u>S31–32</u>, mutual interconversions were observed between **A** (all-[6,6]) and a mixture of **B-1** and **2** (both all-[6,6]) at room temperature, suggesting that one of the addition sites of these

adducts was presumably in an adjacent position and has similar stability. Related mutual isomerization was observed in  $Gd_3N@C_{80}$  adducts (between all-[6,6]-**E** with identical vis-NIR to **A** and all-[6,6]-**G** with identical vis-NIR to **B-1**) (Figures 7c,d and S35i,iii) at room temperature, but more slowly. No isomerization was observed in tris-adduct **C** ([6,6][6,6][5,6]) and tetra-adduct **D** (all-[6,6]) (Figures S33 and 34) for  $Y_3N@C_{80}$  and tris-**F** (unknown addition pattern), **H** ([6,6][6,6][5,6]), and tetra **I** (all-[6,6]) for  $Gd_3N@C_{80}$  at room temperature, indicating their higher stability (Figures S35ii, 36, and 37).

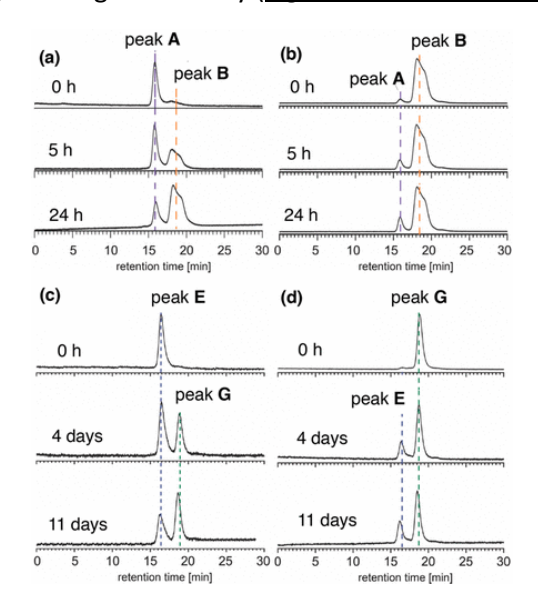


Figure 7. HPLC traces of mutual isomerization between tris-adducts **A** and **B** ( $\mathbf{1} + \mathbf{2}$ ) of  $Y_3N@C_{80}$  (a, b) and between tris-adducts **E** and **G** of  $Gd_3N@C_{80}$  (c, d) in toluene at room temperature. Column: 5PBB 4.6 mm i.d. × 250 mm; solvent: toluene-pyridine (99:1); flow rate: 1.0 mL/min; detection: 390 nm.

Interestingly, the thermal stability of tris-adducts for both TNE-EMF was lower compared to bis-adducts. In case of  $Gd_3N@C_{80}$ , the major-bis-1 was stable at 130 °C for 72 h,(20) while the major-tris **E** and **G** (derivatives from major-bis-1) isomerize at room temperature over a similar time range (Figure S35i,iii). Taken together, the previous reports on the stability of major-bis-adduct of  $Y_3N@C_{80}$ , that was much less stable than major-bis-adduct of  $Gd_3N@C_{80}$ ,(20) we speculated that the relative size of metal cluster and inner cage space may be related to the stability of adducts. The  $Y_3N@C_{80}$  bis-adduct with a smaller metal cluster was less stable compared to the analogous bis-adduct of  $Gd_3N@C_{80}$  with a larger metal cluster.  $Gd_3N@C_{80}$  bis-adduct with a smaller inner cage size was more stable than  $Gd_3N@C_{80}$  tris-adducts with a larger inner size due to three sp³ addition site.

## **Computational Studies**

The experimentally observed regioselectivity toward tris- and tetra-adducts formation for both Gd- and Y-based EMFs is remarkable given the large number of potential addition sites for tris- and tetra-adduct formation. Such a high number of potential adducts, together with the previous observation that isomerizations between Prato adducts can take place via sigmatropic rearrangement at the experimental conditions, (24,31) makes the computational exploration of the most favorable addition site for tris- and

tetra-adduct formation highly challenging. However, in previous studies, we demonstrated that, in EMFs containing large TNT clusters (such as  $Gd_3N$ ), pyramidalization angles of  $sp^2$  cage carbons can be used to predict the most favorable addition sites for the regioselective formation of adducts. (20,21) To discuss such origins of the high regioselectivity of the 1,3-dipolar cycloaddition toward tris- and tetra-adducts formations, DFT calculations were performed.

On the basis of previous DFT calculations on bis-adduct formation, (20,24) we suggested that the major bis-adduct-**2** from Gd<sub>3</sub>N@C<sub>80</sub> corresponds to an asymmetric [6,6][6,6]-isomer at bonds [94–95] and [57–58], while the minor bis-adduct was characterized by X-ray and corresponds to [94–95] and [53–54] additions. The analysis of pyramidalization angles of the DFT-optimized major bis-adduct-**1** of Gd<sub>3</sub>N@C<sub>80</sub>, direct precursor for tris-adducts, was performed on sp<sup>2</sup> C<sub>80</sub> cage carbon, which indicates that the region composed by carbons 20, 22, and 74 (see <u>Figure 8</u> and <u>Table S1</u>) presents the highest pyramidalization angles with the most strain, being highly reactive, and thus tris-adduct functionalization on this region was highly expected. In total, more than 55 different Gd<sub>3</sub>N@C<sub>80</sub> tris-adduct isomers were computationally evaluated. As results, Prato tris-adducts with a third addition site on either [20–22] ([6,6]), [22–23] ([6,6]), [20–74] ([5,6]), [20–16] ([5,6]), [74–73] ([6,6]), or [22–21] ([6,6]) present favorable relative stabilities (see <u>Figure 8</u>) possibly corresponding to peaks **E** and **G**. Considering the experimental results that the isomers in peaks **E** and **G** were all-[6,6] tris structures, structures <u>i</u> ([20–22],  $\Delta E$  = 3.7 kcal/mol), <u>ii</u> ([22–23],  $\Delta E$  = 4.6 kcal/mol), <u>iii</u> ([22–21],  $\Delta E$  = 5.6 kcal/mol), and iv ([74–73],  $\Delta E$  = 4.6 kcal/mol) were thought to be possible structures corresponding to peaks **E** and **G**.

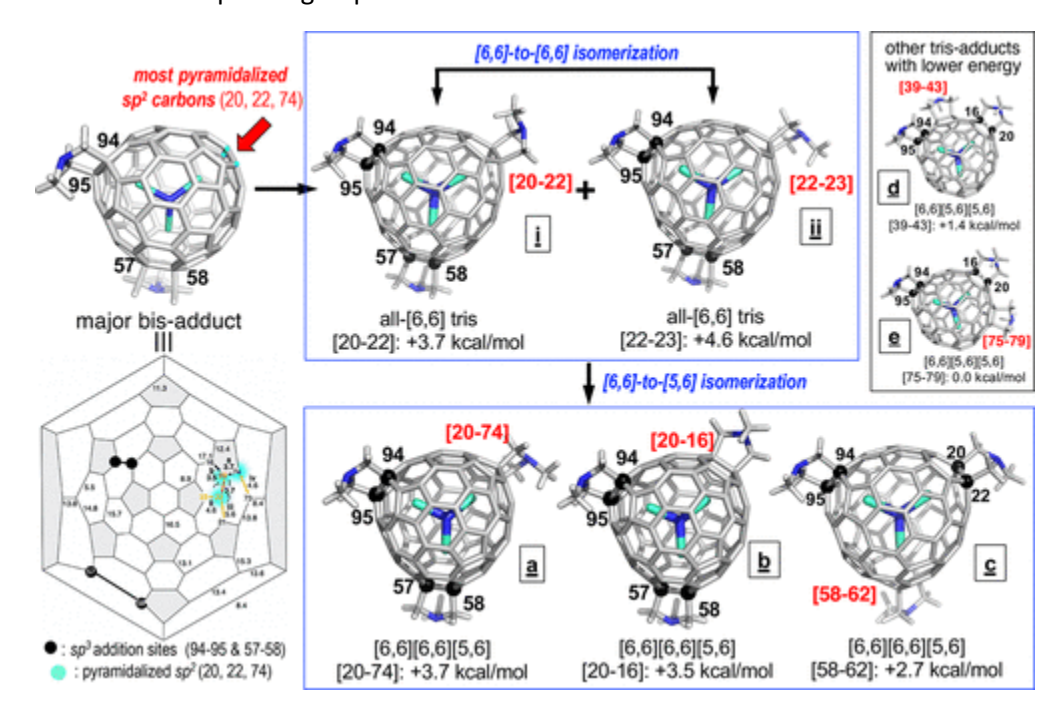


Figure 8. DFT optimized structure and corresponding Schlegel diagram of major bis-adduct (addition sites: [94–95] and [57–58] bonds) for  $Gd_3N@C_{80}$  with  $sp^2$  carbons highlighted with a red arrow and cyan corresponding to the most pyramidalized region (carbons 20, 22, 74) and predicted kinetic tris-adducts (all-[6,6], i and ii) and further obtained thermodynamic tris-adduct ([6,6][6,6][5,6],  $\underline{a} - \underline{c}$ ) via 1,5-sigmatropic rearrangement with DFT-calculated relative stabilities of the different tris-adducts (given in kcal/mol with respect to the lowest in energy tris-adduct e ([6,6][5,6][5,6]).

From the isomerization experiments (<u>Figure 7</u>c,d), it was shown that isomers in peaks **E** and **G** interconvert in equilibrium. Among structures  $\underline{\mathbf{i}}-\underline{\mathbf{i}}\mathbf{v}$ , such isomerization was thought to be possible between  $\underline{\mathbf{i}}$  ([20–22]) and  $\underline{\mathbf{ii}}$  ([22–23]) based on the small energy differences (ca. 1 and 2 kcal/mol, respectively) and their vicinal location, similar to mono and bis-adduct isomerizations.(24,31) The isomerization from  $\underline{\mathbf{i}}\mathbf{v}$  ([74–73]) to  $\underline{\mathbf{i}}$  ([20–22]) is less likely to take place given the stability of intermediate  $\underline{\mathbf{a}}$  with [20–74] bond, which yields a [6,6][6,6][5,6] tris-adduct (<u>Figure 8</u>), equally stable as the all-[6,6]  $\underline{\mathbf{i}}$  ([20–22]). The adjacent [5,6] bond on [20–16] also gives a stable [6,6][6,6][5,6] tris-adduct  $\underline{\mathbf{b}}$  ( $\Delta E$  = 3.5 kcal/mol). These [6,6][6,6][5,6]-tris-adducts  $\underline{\mathbf{a}}$  and  $\underline{\mathbf{b}}$  could potentially correspond to the experimentally observed  $\mathbf{F}$  or [6,6][6,6][5,6]-H peak.

Alternatively, in the tris-adduct  $\underline{\mathbf{i}}$ , isomerization in bond [57–58] to the adjacent [58–52] can yield a ca. 1 kcal/mol more stable [6,6][6,6][5,6]-tris-adduct  $\underline{\mathbf{c}}$  (Figure 8). This adduct  $\underline{\mathbf{c}}$  may also correspond to experimentally observed  $\mathbf{F}$  and  $\mathbf{H}$  peaks. Our DFT calculations also indicate that, among all addition sites considered, the most stable tris-adducts were  $\underline{\mathbf{d}}$  and  $\underline{\mathbf{e}}$  with [6,6][5,6][5,6] structures with addition sites on [39–43] bond (ca.  $\Delta E = 1.4$  kcal/mol) or [75–79] bond (most stable computed tris-adduct), close to the initial addition sites (Figure 8).

Based on the experimental evidence that tetra-adducts are also observed in the presence of tris-adducts, we hypothesized that some of the above-mentioned stable tris-adducts could be further functionalized for formation of the tetra-adduct. Given the large number of possible addition sites, we analyzed the pyramidalization angles of all C–C bonds on the thermodynamically stable tris-adducts (see <u>Table S2</u>):  $\underline{\mathbf{i}}$  (+3.7 kcal/mol),  $\underline{\mathbf{ii}}$  (+4.6 kcal/mol),  $\underline{\mathbf{c}}$  (+2.7 kcal/mol),  $\underline{\mathbf{d}}$  (+1.4 kcal/mol), and  $\underline{\mathbf{e}}$  (0.0 kcal/mol) (see <u>Table S2</u>). Interestingly, the lowest in energy tris-adducts  $\underline{\mathbf{e}}$  (0.0 kcal/mol),  $\underline{\mathbf{d}}$  (+1.4 kcal/mol), and  $\underline{\mathbf{c}}$  (+2.7 kcal/mol) yielded the largest pyramidalization angles, thus suggesting favorable tetra-adduct formation (smaller angles are observed in the case of  $\underline{\mathbf{i}}$  and  $\underline{\mathbf{ii}}$ , see <u>Table S2</u>). Based on NMR data of Y<sub>3</sub>N@C<sub>80</sub> adduct, with identical vis-NIR spectrum of Gd<sub>3</sub>N@C<sub>80</sub> tetra-adduct, the experimentally observed tetra-adduct was with all-[6,6] additions. This fact, taken together with the pyramidalization angle analysis, reduced the number of possible tetra-adducts to consider computationally. From  $\underline{\mathbf{c}}$ ,  $\underline{\mathbf{d}}$ , and  $\underline{\mathbf{e}}$ , all-[6,6] tetra-adducts were constructed based on the most pyramidalized areas and considering the possible isomerization between adjacent bonds (a total of 20 tetra-adducts were studied).

The computed DFT relative stabilities revealed large energy differences of up to ca. 40 kcal/mol among adducts (see <u>Table S3</u>) and provided as the lowest in energy the <u>c</u>-based tetra-adduct corresponding to the addition on bonds [95–94], [20–22], [51–49], and [57–58] (structure <u>c-1</u> in <u>Figure 9</u>). This finding suggests that after initial formation of <u>c</u> [5,6][6,6][6,6] tris-adduct, further Prato functionalization could take place on the [6,6]-junction of [51–49] site, followed by isomerization from the [5,6]-bond ([58–62]) toward the adjacent [6,6] 58–57 yielding the all-[6,6] tetra-adduct <u>c-1</u>. Another possible tetra-adduct from <u>c</u> corresponds to the Prato addition on [53–54], followed by isomerization from the [5,6]-bond ([58–62]) to the adjacent [6,6] ([61–62]). This tetra-adduct <u>c-2</u> ([95–94], [20–22], [61–62], [53–54]) is ca. 6.7 kcal/mol higher in energy than <u>c-1</u>. Interestingly, the tetra-adducts from <u>d</u> and <u>e</u> that share three functionalized sites with <u>c-2</u> (i.e., bonds [95–94], [20–22], [61–62]) present similar relative stabilities of ca. 6 kcal/mol: <u>d-1</u> is ca. 6.3 kcal/mol higher in energy and has the fourth addition on bond [79–78], and <u>e-</u> 1 is ca. 5.7 kcal/mol and has the fourth addend on bond [42–43] (Figure 9).

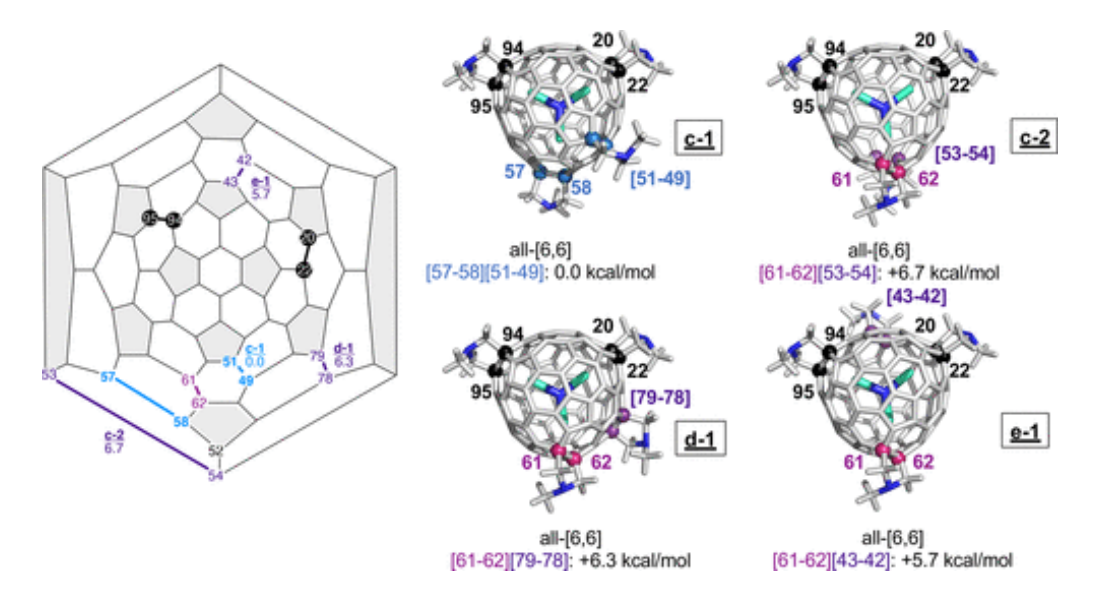


Figure 9. DFT optimized structures of lowest in energy tetra-adducts studied in the present work (in kcal/mol) and corresponding Schlegel diagram: The lowest in energy tetra-adduct computed <u>c-1</u> corresponds to the Prato addition to bonds [95–94], [20–22], (shown in black), and [57–58], [51–49] (in blue), whereas <u>c-2</u>, <u>d-1</u>, and <u>e-1</u> correspond to the addition to bonds [95–94], [20–22] (shown in black), [61–62] (purple), and either [53–54] (<u>c-2</u>), [79–78] (<u>d-1</u>), or [42–43] (<u>e-1</u>).

The DFT relative stabilities, together with the pyramidalization angle analysis and NMR assignments, suggest that tetra-adduct formation is favored to occur from the most stable tris-adducts ( $\underline{c}$ ,  $\underline{d}$ , and  $\underline{e}$ ). This is in line with the fact that computationally characterized lower in energy tris-adducts do not coincide with the experimental assignments based on NMR data. The large energy differences obtained for all analyzed tetra-adducts (that differ up to ca. 40 kcal/mol) are consistent with the high regioselectivity toward tetra-adduct formation observed experimentally, demonstrating that strain release of the most pyramidalized regions of the tris-adducts is the driving force behind the high regioselective tetra-adduct formation.

#### ESR study of bis- and tris-adducts of Gd<sub>3</sub>N@C<sub>80</sub>

From the isomerization results above, we speculated that there is a relationship between the stability of the adducts and the size of endohedral metal cluster relative to the inner space of  $C_{80}$  cage. Especially in the case of  $Gd_3N@C_{80}$ , the cycloaddition to  $C_{80}$  cage provides a longer inner space to better host an endohedral  $Gd_3N$  cluster, which presumably stabilizes and freezes the rotation. In our previous study on the X-ray structure of Prato bis-adduct of  $Gd_3N@C_{80}$ , we showed that two Gd atoms are coordinated to two sp<sup>3</sup> [6,6]-addition sites occupying the extended inner space of  $C_{80}$  cage, which presumably stopped the rotation.

We investigate this situation by comparing ESR spectra of the pristine  $Gd_3N@C_{80}$  and its bis- and trisadducts. Previously, high-frequency (210 and 315 GHz) ESR spectra of  $Gd_3N@C_{80}$  were reported at varied temperatures by Jánossy and co-workers. (48) They interpreted the observed ESR spectra as the signature of three strongly coupled Gd(III) paramagnetic ions with the total spin of S = 21/2. For a paramagnetic center with half-integer spin (so-called Kramers case), the transition between  $m_s = \pm 1/2$  states was

degenerated in zero magnetic field and thus detectable in an ESR experiment at any microwave (m.w.) band. At 210 K and 315 GHz m.w. frequency, the Jánossy group detected a narrow line at the Gd(III) g-factor position (g<sub>Gd</sub> 1.995), which was observed to be narrowed, presumably due to the cluster motion inside the C<sub>80</sub> cage, which was, according to their interpretation, present at least down to the temperature of 50 K. Here, we performed temperature-dependent X-band ESR measurements (9.5 GHz m.w. frequency) on the pristine  $Gd_3N@C_{80}$  and its bis- and tris-adducts. Due to their limited amounts, the bis- and tris-adducts were used as mixtures.

The X-band ESR data for the pristine  $Gd_3N@C_{80}$  showed a narrow single line at q = 1.995 at higher temperatures, and its gradual disappearance at lower temperatures (Figure 10a) is in good agreement to a previous study by Jánossy. Interestingly, for the bis-adduct, the intensity of the narrow EPR line at q =1.995 became weaker with simultaneous appearance of a broad anisotropic ESR line with much larger overall intensity (Figure 10b). Note that by decreasing the temperature from 275 to 150 K, the intensity of lines gradually decreased for Gd<sub>3</sub>N@C<sub>80</sub> (Figure 10a), while it did not change for both bis- and trisadducts (Figures S39 and 40). This strongly suggests that, in the case of the Prato bis-adduct, the rotational mobility of the Gd₃N cluster inside the cage is reduced. In the ESR spectrum of the tris-adduct, no narrow lines were observed anymore. A broader and relatively weaker ESR signal for this tris-adducts sample was hypothesized to be due to a small fraction of Gd₃N clusters undertaking restricted rotational motion, while the main fraction of Gd<sub>3</sub>N clusters is not rotating anymore and their anisotropic ESR signal is out of the reach for the X-band ESR experiment. Jánossy discussed that the ferromagnetic coupling between in three Gd(III) ions would break around 20 K forming three Gd(III) centers with S = 7/2 and weaker zero-field splitting (ZFS) anisotropy. It is likely that ZFS parameters in such a system would be distributed according to the different geometries of the Gd<sub>3</sub>N cluster inside the cage, and the fraction of Gd(III) ions with weakest ZFS might be another possible origin of the ESR signal for the tris-adduct. Regardless of the particular interpretation of the ESR signal for the tris-adduct, our present study strongly suggested that Prato functionalization of the C<sub>80</sub> cage leads to deactivation of the Gd<sub>3</sub>N cluster rotational tumbling at ambient temperature.

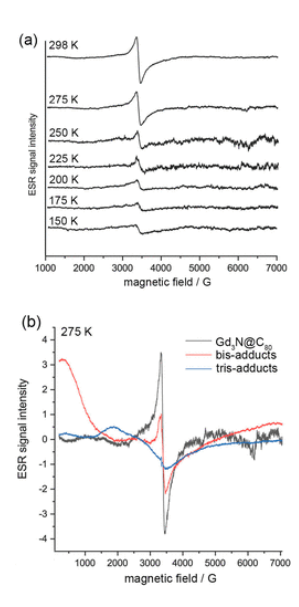


Figure 10. (a) 9.5 GHz EPR spectra of  $Gd_3N@C_{80}$  at various temperatures and (b) bis **1** and tris-adducts **E**–**G** at 275 K.

## Discussion on the Origin of the Regioselectivity

As described above, bis-1,3-dipolar cycloaddition does not proceed regioselectively in the case of empty  $I_h$ - $C_{60}$ , and it is reasonable to conclude that the observed high regioselectivity in the generation of bis-, tris-, and tetra-adducts in  $Y_3N@C_{80}$  and  $Gd_3N@C_{80}$  reported in this study was due to the effect of the encapsulated endohedral metal cluster inside  $I_h$ - $C_{80}$ . In general, the regioselectivity in cycloaddition reactions involving fullerenes is explained by the pyramidalization angle of  $sp^2$  cage carbons; addition is favored to the most pyramidalized  $sp^2$  carbons with strain which is released after reaction by the formation of  $sp^3$  carbon. This situation is particularly observed in the cycloaddition to  $C_{70}$  having several types of  $sp^2$  carbons with different pyramidalization angles. In the case of TNT-EMF, molecules containing relatively large metal clusters ( $M_3N$ , M = Y, Gd), they are known to induce strain on the fullerene cage carbon structure and pyramidalize specific regions of it to impact the fullerene exohedral reactivity.

In the previous studies, mono-Prato reactions were shown to produce kinetic [6,6]-adducts, which isomerized to [5,6]-adducts in a rate and a ratio dependent on the metal cluster size. The [6,6]-adduct, which is stable in the presence of larger  $M_3N$  clusters (M=Y, Gd), can produce bis-[6,6][6,6]-adducts in a high regioselective manner. This is due to the activation of certain  $sp^2$  cage carbons, which is pyramidalized by the effect of metals, one of which is accommodated by the inner space of initial  $sp^3$  addition site and the other one directs for the activation of second addition. This situation, a sort of host (internal concave space of  $C_{80}$  monoadduct)—guest (one of the metal cation) interaction, was clearly observed in the X-ray structure of minor-bis-adduct of  $Gd_3N@C_{80}$  in the previous study.

In the tris- and tetra-addition reactions in this study, pyramidalization of the  $C_{80}$  cage carbon was the main factor for cause of regioselectivity. When using the bis-adduct as a precursor of tris-adduct formation, two metals of  $M_3N$  are already accommodated to the inside of  $sp^3$  addition site, simultaneously allowing the endohedral  $M_3N$  cluster to be flattened. As one evidence in this study, the ESR spectra indicated reduced rotational mobility of the metal cluster inside the bis- and tris-adducts in comparison to the pristine  $Gd_3N@C_{80}$  presumably because of the interaction of internal  $C_{80}$  cavity to the metal. In the bis-adduct, the strain of the entire molecule is partially released because of the flattened  $M_3N$  cluster, and couple of particular  $sp^2$  carbons are activated by the third metal (not pointing to any  $sp^3$  addition site yet). In comparison to the bis-addition, tris-addition provided more regioisomers presumably because the  $sp^3$  cluster inside the  $sp^3$  cage is less pyramidalized and activation of last  $sp^2$  addition site was less effective.

An interesting result is the generation of tetra-addition with a single major adduct (all-[6,6]), which was hard to evaluate due to its complex structure and the high number of possible isomers. However, the combination of NMR, vis-NIR, pyramidalization angle analysis, and DFT calculations indicates that the driving force behind the high regioselectivity is strain-release of the most pyramidalized fullerene regions. DFT indicated that the most stable tris-adducts present considerably higher pyramidalization angles in the area surrounding the third metal cluster where none of the three previous Prato additions took place. This high pyramidalization favors the subsequent Prato addition for tetra-adduct formation, leading to a high regioselectivity of the process. This is also supported by the large energy differences obtained among tetra-adducts.

## Conclusion

Exhaustive Prato cycloadditions to the endohedral metallofullerenes,  $Y_3N@C_{80}$  and  $Gd_3N@C_{80}$ , provided tris- and tetra-adducts in a highly regioselective manner. By  $^1H$  and  $^{13}C$  NMR analyses of the adducts of

 $Y_3N@C_{80}$ , in combination with the vis-NIR spectra and DFT calculations, the addition patterns of tris- and tetra-adducts were elucidated. By isomerization and ESR studies, the motion of the endohedral clusters was estimated in relation to the numbers of the functionalization affecting the stability of the derivatives. The ability to form these unique fullerene adducts and their distinct physiochemical properties will be of great value in designing new TNT-EMF-based materials.

#### **Supporting Information**

The Supporting Information is available free of charge at <a href="https://pubs.acs.org/doi/10.1021/jacs.9b13768">https://pubs.acs.org/doi/10.1021/jacs.9b13768</a>.

Detailed protocol of Prato reactions and HPLC analysis, spectroscopic data of adducts, and detail
of ESR measurements (<u>PDF</u>)

## Corresponding Authors

- Sílvia Osuna Institut de Química Computacional i Catàlisi (IQCC) and Departament de Química, Universitat de Girona, Maria Aurelia Capmany 69, 17003 Girona, Catalonia, Spain; ICREA, Pg. Lluís Companys 23, 08010 Barcelona, Catalonia, Spain; <a href="http://orcid.org/0000-0003-3657-6469">http://orcid.org/0000-0003-3657-6469</a>; Email: <a href="mailto:silvia.osuna@udg.edu">silvia.osuna@udg.edu</a>
- Yoko Yamakoshi Laboratorium für Organische Chemie, ETH Zürich, Vladimir-Prelog-Weg 3, 8093 Zürich, Switzerland; <a href="http://orcid.org/0000-0001-8466-0118">http://orcid.org/0000-0001-8466-0118</a>; Email: <a href="mailto:yamakoshi@org.chem.ethz.ch">yamakoshi@org.chem.ethz.ch</a>

# Authors

- Olesya Semivrazhskaya Laboratorium für Organische Chemie, ETH Zürich, Vladimir-Prelog-Weg 3, 8093 Zürich, Switzerland
- Safwan Aroua Laboratorium für Organische Chemie, ETH Zürich, Vladimir-Prelog-Weg 3, 8093 Zürich, Switzerland
- Maxim Yulikov Laboratorium für Physikalische Chemie, ETH Zürich, Vladimir-Prelog-Weg
   1, 8093 Zürich, Switzerland; <a href="http://orcid.org/0000-0003-3275-0714">http://orcid.org/0000-0003-3275-0714</a>
- Adrian Romero-Rivera Institut de Química Computacional i Catàlisi (IQCC) and Departament de Química, Universitat de Girona, Maria Aurelia Capmany 69, 17003 Girona, Catalonia, Spain
- Steven Stevenson Department of Chemistry, Purdue University Fort Wayne, Fort Wayne, Indiana 46805, United States; <a href="http://orcid.org/0000-0003-3576-4062">http://orcid.org/0000-0003-3576-4062</a>
- Marc Garcia-Borràs Institut de Química Computacional i Catàlisi (IQCC) and Departament de Química, Universitat de Girona, Maria Aurelia Capmany 69, 17003 Girona, Catalonia, Spain; http://orcid.org/0000-0001-9458-1114
- **Notes** The authors declare no competing financial interest.

## **Acknowledgments**

The authors thank Prof. Dr. Gunnar Jeschke at ETH for his help on ESR measurements. The authors thank Prof. Dr. François Diederich at ETH for his fruitful discussion. The authors thank NMR service and MoBiAS in the LOC at ETH Zürich for their NMR and MS measurements. This study was supported in part by the Swiss National Foundation (200021\_156097, 205321\_17318, IZLJZ2\_183660, Y.Y.), the ETH Research Grant (ETH-21 15-2, ETH-25 11-1, Y.Y.), and National Science Foundation (1856461, S.S.). This study was also supported in part by the European Research Council Horizon 2020 research and innovation program (ERC-2015-StG-679001, S.O.), Spanish MINECO (project PGC2018-102192-B-I00, S.O.; and Juan de la Cierva - Incorporación fellowship IJCI-2017-33411, M.G.-B.), and Generalitat de Catalunya AGAUR (SGR-1707, S.O.; and Beatriu de Pinós H2020 MSCA-Cofund 2018-BP-00204, M.G.-B.).

#### References

- 1. Ross, R. B.; Cardona, C. M.; Guldi, D. M.; Sankaranarayanan, S. G.; Reese, M. O.; Kopidakis, N.; Peet, J.; Walker, B.; Bazan, G. C.; Van Keuren, E.; Holloway, B. C.; Drees, M. Endohedral fullerenes for organic photovoltaic devices. Nat. Mater. 2009, 8 (3), 208–212, DOI: 10.1038/nmat2379
- Zhang, J. F.; Fatouros, P. P.; Shu, C. Y.; Reid, J.; Owens, L. S.; Cai, T.; Gibson, H. W.; Long, G. L.; Corwin, F. D.; Chen, Z. J.; Dorn, H. C. High Relaxivity Trimetallic Nitride (Gd3N) Metallofullerene MRI Contrast Agents with Optimized Functionality. Bioconjugate Chem. 2010, 21 (4), 610–615, DOI: 10.1021/bc900375n
- 3. Han, Z.; Wu, X.; Roelle, S.; Chen, C.; Schiemann, W. P.; Lu, Z. R. Targeted gadofullerene for sensitive magnetic resonance imaging and risk-stratification of breast cancer. Nat. Commun. 2017, 8 (1), 692, DOI: 10.1038/s41467-017-00741-y
- 4. Bolskar, R. D. Gadofullerene MRI contrast agents. Nanomedicine 2008, 3 (2), 201–13, DOI: 10.2217/17435889.3.2.201
- 5. Li, T.; Xiao, L.; Yang, J.; Ding, M.; Zhou, Z.; LaConte, L.; Jin, L.; Dorn, H. C.; Li, X. Trimetallic Nitride Endohedral Fullerenes Carboxyl-Gd3N@C80: A New Theranostic Agent for Combating Oxidative Stress and Resolving Inflammation. ACS Appl. Mater. Interfaces 2017, 9 (21), 17681–17687, DOI: 10.1021/acsami.7b04718
- Shu, C.; Corwin, F. D.; Zhang, J.; Chen, Z.; Reid, J. E.; Sun, M.; Xu, W.; Sim, J. H.; Wang, C.; Fatouros, P. P.; Esker, A. R.; Gibson, H. W.; Dorn, H. C. Facile preparation of a new gadofullerene-based magnetic resonance imaging contrast agent with high 1H relaxivity. Bioconjugate Chem. 2009, 20 (6), 1186–93, DOI: 10.1021/bc900051d
- 7. Kang, H.; Lee, W.; Oh, J.; Kim, T.; Lee, C.; Kim, B. J. From Fullerene-Polymer to All-Polymer Solar Cells: The Importance of Molecular Packing, Orientation, and Morphology Control. Acc. Chem. Res. 2016, 49 (11), 2424–2434, DOI: 10.1021/acs.accounts.6b00347
- 8. Cardona, C. M.; Elliott, B.; Echegoyen, L. Unexpected chemical and electrochemical properties of M3N@C80 (M = Sc, Y, Er). J. Am. Chem. Soc. 2006, 128 (19), 6480–6485, DOI: 10.1021/ja061035n

- 9. Popov, A. A.; Yang, S.; Dunsch, L. Endohedral fullerenes. Chem. Rev. 2013, 113 (8), 5989–6113, DOI: 10.1021/cr300297r
- 10. lezzi, E. B.; Duchamp, J. C.; Harich, K.; Glass, T. E.; Lee, H. M.; Olmstead, M. M.; Balch, A. L.; Dorn, H. C. A symmetric derivative of the trimetallic nitride endohedral metallofullerene, Sc3N@C80. J. Am. Chem. Soc. 2002, 124 (4), 524–525, DOI: 10.1021/ja0171005
- 11. Cardona, C. M.; Kitaygorodskiy, A.; Ortiz, A.; Herranz, M. A.; Echegoyen, L. The first fulleropyrrolidine derivative of Sc3N@C80: Pronounced chemical shift differences of the geminal protons on the pyrrolidine ring. J. Org. Chem. 2005, 70 (13), 5092–5097, DOI: 10.1021/jo0503456
- 12. Lukoyanova, O.; Cardona, C. M.; Rivera, J.; Lugo-Morales, L. Z.; Chancellor, C. J.; Olmstead, M. M.; Rodriguez-Fortea, A.; Poblet, J. M.; Balch, A. L.; Echegoyen, L. "Open rather than closed" malonate methano-fullerene derivatives. The formation of methanofulleroid adducts of Y3N@C80. J. Am. Chem. Soc. 2007, 129 (34), 10423–10430, DOI: 10.1021/ja071733n
- 13. Cai, T.; Slebodnick, C.; Xu, L.; Harich, K.; Glass, T. E.; Chancellor, C.; Fettinger, J. C.; Olmstead, M. M.; Balch, A. L.; Gibson, H. W.; Dorn, H. C. A pirouette on a metallofullerene sphere: Interconversion of isomers of N-tritylpyrrolidino Ih Sc3N@C80. J. Am. Chem. Soc. 2006, 128 (19), 6486–6492, DOI: 10.1021/ja0601843
- 14. Stevenson, S.; Stephen, R. R.; Amos, T. M.; Cadorette, V. R.; Reid, J. E.; Phillips, J. P. Synthesis and purification of a metallic nitride fullerene bisadduct: exploring the reactivity of Gd3N@C80. J. Am. Chem. Soc. 2005, 127 (37), 12776–7, DOI: 10.1021/ja0535312
- 15. Cai, T.; Xu, L.; Shu, C.; Champion, H. A.; Reid, J. E.; Anklin, C.; Anderson, M. R.; Gibson, H. W.; Dorn, H. C. Selective formation of a symmetric Sc3N@C78 bisadduct: adduct docking controlled by an internal trimetallic nitride cluster. J. Am. Chem. Soc. 2008, 130 (7), 2136–7, DOI: 10.1021/ja077630m
- 16. Feng, L.; Tsuchiya, T.; Wakahara, T.; Nakahodo, T.; Piao, Q.; Maeda, Y.; Akasaka, T.; Kato, T.; Yoza, K.; Horn, E.; Mizorogi, N.; Nagase, S. Synthesis and characterization of a bisadduct of La@C82. J. Am. Chem. Soc. 2006, 128 (18), 5990–1, DOI: 10.1021/ja058390i
- 17. Ishitsuka, M. O.; Sano, S.; Enoki, H.; Sato, S.; Nikawa, H.; Tsuchiya, T.; Slanina, Z.; Mizorogi, N.; Liu, M. T.; Akasaka, T.; Nagase, S. Regioselective bis-functionalization of endohedral dimetallofullerene, La2@C80: extremal La-La distance. J. Am. Chem. Soc. 2011, 133 (18), 7128–34, DOI: 10.1021/ja200903q
- 18. Lu, X.; Nikawa, H.; Tsuchiya, T.; Maeda, Y.; Ishitsuka, M. O.; Akasaka, T.; Toki, M.; Sawa, H.; Slanina, Z.; Mizorogi, N.; Nagase, S. Bis-carbene adducts of non-IPR La2@C72: localization of high reactivity around fused pentagons and electrochemical properties. Angew. Chem., Int. Ed. 2008, 47 (45), 8642–5, DOI: 10.1002/anie.200803529
- 19. Sawai, K.; Takano, Y.; Izquierdo, M.; Filippone, S.; Martin, N.; Slanina, Z.; Mizorogi, N.; Waelchli, M.; Tsuchiya, T.; Akasaka, T.; Nagase, S. Enantioselective synthesis of endohedral metallofullerenes. J. Am. Chem. Soc. 2011, 133 (44), 17746–52, DOI: 10.1021/ja2062727

- 20. Aroua, S.; Garcia-Borras, M.; Bolter, M. F.; Osuna, S.; Yamakoshi, Y. Endohedral metal-induced regioselective formation of bis-Prato adduct of Y3N@Ih-C80 and Gd3N@Ih-C80. J. Am. Chem. Soc. 2015, 137 (1), 58–61, DOI: 10.1021/ja511008z
- 21. Ceron, M. R.; Izquierdo, M.; Garcia-Borras, M.; Lee, S. S.; Stevenson, S.; Osuna, S.; Echegoyen, L. Bis-1,3-dipolar Cycloadditions on Endohedral Fullerenes M3N@Ih-C80 (M = Sc, Lu): Remarkable Endohedral-Cluster Regiochemical Control. J. Am. Chem. Soc. 2015, 137 (36), 11775—11782, DOI: 10.1021/jacs.5b07207
- 22. Ceron, M. R.; Maffeis, V.; Stevenson, S.; Echegoyen, L. Endohedral fullerenes: Synthesis, isolation, mono- and bis-functionalization. Inorg. Chim. Acta 2017, 468, 16–27, DOI: 10.1016/j.ica.2017.03.040
- 23. Ceron, M. R.; Echegoyen, L. Recent progress in the synthesis of regio-isomerically pure bis-adducts of empty and endohedral fullerenes. J. Phys. Org. Chem. 2016, 29 (11), 613–619, DOI: 10.1002/poc.3563
- 24. Semivrazhskaya, O.; Romero-Rivera, A.; Aroua, S.; Troyanov, S. I.; Garcia-Borras, M.; Stevenson, S.; Osuna, S.; Yamakoshi, Y. Structures of Gd3N@C80 Prato Bis-Adducts: Crystal Structure, Thermal Isomerization, and Computational Study. J. Am. Chem. Soc. 2019, 141 (28), 10988–10993, DOI: 10.1021/jacs.9b05603
- 25. Kordatos, K.; Bosi, S.; Da Ros, T.; Zambon, A.; Lucchini, V.; Prato, M. Isolation and characterization of all eight bisadducts of fulleropyrrolidine derivatives. J. Org. Chem. 2001, 66 (8), 2802–2808, DOI: 10.1021/jo001708z
- 26. Lu, Q.; Schuster, D. I.; Wilson, S. R. Preparation and characterization of six bis(N-methylpyrrolidine)-C60 isomers: Magnetic deshielding in isomeric bisadducts of C60. J. Org. Chem. 1996, 61 (14), 4764–4768, DOI: 10.1021/jo960466t
- 27. More recently, Echegoyen group reported the generation of two minor symmetric bis-adducts ([5,6][5,6] and [5,6][6,6]) of Y3N@C80.
- 28. Stevenson, S.; Phillips, J. P.; Reid, J. E.; Olmstead, M. M.; Rath, S. P.; Balch, A. L. Pyramidalization of Gd3N inside a C80 cage. The synthesis and structure of Gd3N@C80. Chem. Commun. 2004, 24, 2814–5, DOI: 10.1039/b412338g
- 29. Echegoyen, L.; Chancellor, C. J.; Cardona, C. M.; Elliott, B.; Rivera, J.; Olmstead, M. M.; Balch, A. L. X-Ray crystallographic and EPR spectroscopic characterization of a pyrrolidine adduct of Y3N@C80. Chem. Commun. 2006, 25, 2653–5, DOI: 10.1039/b604011j
- 30. Aroua, S.; Yamakoshi, Y. Prato Reaction of M3N@Ih-C80 (M = Sc, Lu, Y, Gd) with Reversible Isomerization. J. Am. Chem. Soc. 2012, 134 (50), 20242–20245, DOI: 10.1021/ja309550z
- 31. Aroua, S.; Garcia-Borras, M.; Osuna, S.; Yamakoshi, Y. Essential factors for control of the equilibrium in the reversible rearrangement of M3N@Ih-C80 fulleropyrrolidines: exohedral functional groups versus endohedral metal clusters. Chem. Eur. J. 2014, 20 (43), 14032– 9, DOI: 10.1002/chem.201403743
- 32. Cardona, C. M.; Kitaygorodskiy, A.; Echegoyen, L. Trimetallic nitride endohedral metallofullerenes: Reactivity dictated by the encapsulated metal cluster. J. Am. Chem. Soc. 2005, 127 (29), 10448–10453, DOI: 10.1021/ja052153y

- 33. Echegoyen, L.; Chancellor, C. J.; Cardona, C. M.; Elliott, B.; Rivera, J.; Olmstead, M. M.; Balch, A. L. X-Ray crystallographic and EPR spectroscopic characterization of a pyrrolidine adduct of Y3N@C80. Chem. Commun. 2006, (25), 2653–2655, DOI: 10.1039/b604011j
- 34. Baerends, E. J.; Autschbach, J.; Bérces, A.; Bickelhaupt, F. M.; Bo, C.; de Boeij, P. L.; Boerrigter, P. M.; Cavallo, L.; Chong, D. P.; Deng, L.; Dickson, R. M.; Ellis, D. E.; Fan, L.; Fischer, T. H.; Fonseca Guerra, C.; van Gisbergen, S. J. A.; Groeneveld, J. A.; Gritsenko, O. V.; Grüning, M.; Harris, F. E.; van den Hoek, P.; Jacob, C. R.; Jacobsen, H.; Jensen, L.; an Kessel, G.; Kootstra, F.; van Lenthe, E.; McCormack, D. A.; Michalak, A.; Neugebauer, J.; Osinga, V. P.; Patchkovskii, S.; Philipsen, P. H. T.; Post, D.; Pye, C. C.; Ravenek, W.; Ros, P.; Schipper, P. R. T.; Schreckenbach, G.; Snijders, J. G.; Solà, M.; Swart, M.; Swerhone, D.; te Velde, G.; Vernooijs, P.; Versluis, L.; Visscher, L.; Visser, O.; Wang, F.; Wesolowski, T. A.; van Wezenbeek, E.; Wiesenekker, G.; Wolff, S. K.; Woo, T. K.; Yakovlev, A. L.; Ziegler, T.; ADF2010.1, SCM: Amsterdam, 2010.
- 35. te Velde, G.; Bickelhaupt, F. M.; Baerends, E. J.; Guerra, C. F.; Van Gisbergen, S. J. A.; Snijders, J. G.; Ziegler, T. Chemistry with ADF. J. Comput. Chem. 2001, 22 (9), 931–967, DOI: 10.1002/jcc.1056
- 36. Vosko, S. H.; Wilk, L.; Nusair, M. Accurate Spin-Dependent Electron Liquid Correlation Energies for Local Spin-Density Calculations a Critical Analysis. Can. J. Phys. 1980, 58 (8), 1200–1211, DOI: 10.1139/p80-159
- 37. Becke, A. D. Density-Functional Exchange-Energy Approximation with Correct Asymptotic-Behavior. Phys. Rev. A: At., Mol., Opt. Phys. 1988, 38 (6), 3098–3100, DOI: 10.1103/PhysRevA.38.3098
- 38. Perdew, J. P.; Yue, W. Accurate and Simple Density Functional for the Electronic Exchange Energy Generalized Gradient Approximation. Phys. Rev. B: Condens. Matter Mater. Phys. 1986, 33 (12), 8800–8802, DOI: 10.1103/PhysRevB.33.8800
- 39. vanLenthe, E.; vanLeeuwen, R.; Baerends, E. J.; Snijders, J. G. Relativistic regular two-component Hamiltonians. Int. J. Quantum Chem. 1996, 57 (3), 281–293, DOI: 10.1002/(SICI)1097-461X(1996)57:3<281::AID-QUA2>3.0.CO;2-U
- 40. Grimme, S. Semiempirical GGA-type density functional constructed with a long-range dispersion correction. J. Comput. Chem. 2006, 27 (15), 1787–1799, DOI: 10.1002/jcc.20495
- 41. Grimme, S.; Antony, J.; Ehrlich, S.; Krieg, H. A consistent and accurate ab initio parametrization of density functional dispersion correction (DFT-D) for the 94 elements H-Pu. J. Chem. Phys. 2010, 132, 154104, DOI: 10.1063/1.3382344
- 42. Osuna, S.; Swart, M.; Sola, M. Dispersion Corrections Essential for the Study of Chemical Reactivity in Fullerenes. J. Phys. Chem. A 2011, 115 (15), 3491–3496, DOI: 10.1021/jp1091575
- 43. Garcia-Borras, M.; Osuna, S.; Luis, J. M.; Swart, M.; Sola, M. The Exohedral Diels-Alder Reactivity of the Titanium Carbide Endohedral Metallofullerene Ti2C2@D3h-C78: Comparison with D3h-C78 and M3N@D3h-C78 (M = Sc and Y) Reactivity. Chem. Eur. J. 2012, 18 (23), 7141–7154, DOI: 10.1002/chem.201103701
- 44. Swart, M.; Bickelhaupt, F. M. QUILD: QUantum-regions interconnected by local descriptions. J. Comput. Chem. 2008, 29 (5), 724–734, DOI: 10.1002/jcc.20834

- 45. A similar result was observed by MALDI-MS analyses (Figures S1a and S25a).
- 46. The two tris-adducts of Y3N@C80 in the major peak B could not be separated even by intensive trials using various HPLC columns (5PBB, Buckyprep-M, Buckyprep-D, Buckyprep, Buckyclutcher, PYE) and several solvent systems (toluene-MeCN (99:1, 2:1, 9:1), toluene-pyridine (99:1), toluene-MeOH (99:1), toluene-THF (1:1), toluene-EtOAc (1:1)).
- 47. Rodriguez-Fortea, A.; Campanera, J. M.; Cardona, C. M.; Echegoyen, L.; Poblet, J. M. Dancing on a fullerene surface: Isomerization of Y3N@(N-ethylpyrrolidino-C80) from the 6,6 to the 5,6 regioisomer. Angew. Chem., Int. Ed. 2006, 45 (48), 8176–8180, DOI: 10.1002/anie.200604052
- 48. Nafradi, B.; Antal, A.; Pasztor, A.; Forro, L.; Kiss, L. F.; Feher, T.; Kovats, E.; Pekker, S.; Janossy, A. Molecular and Spin Dynamics in the Paramagnetic Endohedral Fullerene Gd3N@C80. J. Phys. Chem. Lett. 2012, 3 (22), 3291–3296, DOI: 10.1021/jz301250j